Heliyon 10 (2024) e34315

Contents lists available at ScienceDirect

Heliyon

journal homepage: www.cell.com/heliyon

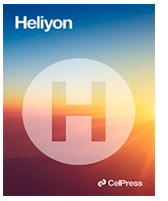

Research article

Microstructural and mechanical characterization of electron beam welded low-nickel nitrogen-strengthened austenitic stainless steel

Ahmad Naseem [a], Muhammad Ilyas [b], Tauheed Shehbaz [c], Ghulam Hussain [d,*], Mohammed Alkahtani [e]

[a] Faculty of Mechanical Engineering, Ghulam Ishaq Khan Institute of Engineering Sciences and Technology, 23640, Topi, Pakistan
[b] Advance Tank Production Ltd, 144 Henderson Drive, Regina, S4N 5P7, SK, Canada
[c] Faculty of Materials and Chemical Engineering, Department of Materials Science, Ghulam Ishaq Khan Institute of Engineering Sciences and Technology, 23640, Topi, Pakistan
[d] Mechanical Engineering Department, College of Engineering, University of Bahrain, Isa Town, 32038, Bahrain
[e] Department of Industrial Engineering, College of Engineering, King Saud University, P.O. Box 800, Riyadh, 11421, Saudi Arabia

ARTICLE INFO

Keywords:
Low-nickel nitrogen-strengthened austenitic stainless steel
E.B.W.
Microstructures mechanical properties

ABSTRACT

In this paper, the Electron Beam Welding (EBW) was used to join thin plates of low-nickel nitrogen-strengthened austenitic stainless steel (LNiASS), a material valued for its superior mechanical properties and cost-effectiveness. Traditional welding techniques often lead to issues such as hot cracking, reduced toughness, and undesirable microstructures. The objective was to address these challenges using EB·W., which offers precise control, minimal heat input, and deeper penetration.

Methodology included joining LNiASS plates with E.B.W. and analyzing the resulting microstructures and mechanical properties through optical microscopy, tensile testing, microhardness testing, and scanning electron microscopy (SEM). The findings indicated the presence of various ferrite morphologies without significant precipitation of deleterious phases like carbides and sigma phase. The weldment strength was ~90 % of the base alloy, with fractures occurring near the weld cord due to nitrogen loss and grain coarsening in the (HAZ). Microhardness increased by ~12.9 %, attributed to microstructural evolution and a fine-grained structure. Impact testing in Charpy V-Notch (CVN) configuration showed the weld absorbed ~50 % more impact energy than the base material, due to refined Microstructure and enhanced hardness. Longitudinal residual stress analysis indicated compressive nature below mid-thickness, resulting from thermal expansion and contraction during welding. These results demonstrated E.B·W.'s effectiveness in preserving mechanical properties and enhancing the performance of nitrogen-strengthened stainless steel welds.

1. Introduction

Austenitic stainless steels are widely utilized in diverse industrial sectors, such as power generation and petrochemicals, due to their ability to synergistically enhance mechanical performance and corrosion resistance [1–4]. Nevertheless, constraints regarding the yield strength threshold inevitably pose obstacles to their broader adoption in various applications. Researchers have been

* Corresponding author. Mechanical Engineering Department, College of Engineering, University of Bahrain, Isa Town, 32038, Bahrain.
E-mail address: ghussain@uob.edu.bh (G. Hussain).

https://doi.org/10.1016/j.heliyon.2024.e34315
Received 14 May 2024; Received in revised form 8 July 2024; Accepted 8 July 2024
Available online 9 July 2024

concentrating on its material behavior and processing, particularly its applications in hydrogen fuel cell technology, biocompatibility, wear resistance, tribological properties, and joining techniques [5,6]. Additionally, efforts have been made to investigate functional grading and dissimilar welding of low-nickel grades with conventional Cr–Ni austenitic stainless steels [7,8].

Obtaining higher yield strengths in austenitic stainless steels through interstitial carbon alloying presents a challenge. Excessive carbon content within the matrix can lead to preferential grain boundary carbide precipitation and chromium depletion, a phenomenon known as sensitization. Sensitization poses a significant issue in high-strength austenitic stainless steel grades [9]. In order to overcome these limitations, derivative of austenitic stainless steels i.e. interstitially Nitrogen alloyed stainless steel offers cardinal acceptability [10,11].

Nitrogen-strengthened austenitic steels (LNiASS) have gained immense attention for various industrial and development objectives. Their high strength and work hardenability, commendable corrosion resistance, deformation-induced martensitic transformation, good fracture toughness, and biocompatibility make them an attractive candidate material for power generation and medical equipment [12], tribology [13] and cryogenic applications.

Nitrogen in austenitic stainless steels has a tremendous effect on stabilizing the austenite phase, thus enabling the partial or complete replacement of expensive and allergenic Ni as an austenite-stabilizing element. Owing to its greater solubility in iron than carbon, Nitrogen solid solution strengthening further enhances mechanical properties, particularly yield strength. Moreover, nitrogen forms stable nitrides, which, when dispersed within the steel matrix, impede dislocation movement, thereby increasing the yield strength of the steel [9].

The joining of nitrogen-strengthened austenitic stainless steels holds significant importance for various industrial applications due to their unique combination of mechanical strength and corrosion resistance properties [14,15]. However, joining of LNiASS presents a significant challenge due to the unique properties imparted by nitrogen alloying. Moreover, traditional fusion welding methods can render them susceptible to formation of various secondary phases, outgassing of alloying elements and desorption of Nitrogen that eventually impairs their mechanical properties as well as overall alloy performance [7]. Dong et al. [16] observed the process of nitrogen desorption and absorption in alloys containing different percentage of Nitrogen during and T.I.G. and CO_2 laser welding and concluded that the N2 desorption is higher during T.I.G. welding. Kumar et al. [17] recently investigated the multi-pass gas metal arc (G.M.A.) welded (0.29 %) Nitrogen bearing austenitic stainless steel and reported carbide precipitation in clusters and bimodal Microstructure containing austenite and ferrite. Moreover, fusion welding techniques can impart significant distortions and built-up stresses [18,19].

High energy beam welding methods including Electron and Laser beam welding prove beneficial in achieving higher welding speeds and narrow fusion zones. Moreover due to comparatively lesser heat inputs these techniques minimize the heat aided distortion, produce narrow heat effected zones (HAZ) and allow lesser micro segregation owing to rapid cooling rates involved [20]. In a similar fashion, rapid cooling rate sets the tendency of carbide precipitation to plummet considerably.

Various authors have pivoted their research upon beam welding and pertaining matters for stainless steels, specifically incorporating austenitic and ferritic grades owing to their widespread applications. The addition of Ni and post weld heat treatment (PWHT) on the T.I.G. welded Duplex and super duplex stainless steel was studied by the authors [21,22] and observed that the equal amount of ferrite and austenite was reinstated with no intermetallic compounds (I.M.C.s). Moreover, addition of Ni enhanced the hardness of the weldment owing to the increased fraction widmanstatten ferrite and austenite. A. Tahaei et al. [23] conducted a comprehensive investigation into the impact of nickel addition and post-weld heat treatment (PWHT) on the corrosion susceptibility of welded duplex stainless steels. Their study revealed that pitting corrosion predominantly initiates and propagates in the heat-affected zone (HAZ), indicating that this region exhibits a higher susceptibility to corrosion compared to the fusion zone. Zhang et al. [24] carried research on fibre laser welding of 5 mm thick 304 austenitic stainless steel to study the effect of laser power, defocusing distance and weld speed on appearance and properties of laser welds. It was concluded that with the aid of appropriate welding parameters in fibre laser welding tensile residual stresses were of lower magnitude as compared to CO_2 and Nd: YAG laser welding. Alali et al. [25] explored the application window of electron beam welding to join 20 mm thick section of 316 L nuclear grade austenitic stainless steel. Defect free joint was accomplished, and a region of high schmid factor intensity was observed at weld centreline that ultimately served as the weakest region. The Fusion zone comprised of columnar and equiaxed grains that caused tensile strength to 650 Mpa. Youmin et al. [26] conducted experiments to study Microstructure, microhardness, distortion and residual stress of 316 L stainless steel in T joint configuration using L.B.W. process. Improved hardness was achieved in the centre of the weld due to the formation of fine equiaxed dendrites. Jun et al. [27] conducted a comparative analysis of the microstructural and mechanical characteristics of 304 grade austenitic stainless steel using both T.I.G. and L.B.W. processes. The findings suggested that L.B.W. enhanced tensile strength in comparison to the traditional T.I.G. method. However, it was observed that excessive heat input during L.B.W. could render austenitic stainless steel vulnerable to sensitization, hot cracking, and grain growth within the HAZ. Ying et al. [28] utilized simulation models of T.I.G. in the Wire Arc Additive Manufacturing (WAAM) process to understand how process parameters affect certain aspects of WAAM quality in carbon steel, focusing on the Microstructure and mechanical properties.

Mukherjee et al. [29] investigated the impact of incorporating three metal transfer modes (Short Circuiting - S·C., Spray, and Pulse) and three variations of austenitic fillers, under two shielding gas mixtures, on the microstructural constituents and mechanical properties of Fe16Cr1Ni9Mn0·12 N austenitic stainless steels. The observations revealed that weld metal with a higher proportion of metastable γ-phase exhibited transformation during severe plastic deformation, resulting in the emergence of α'-martensite along the fracture path. This α'-martensite effectively hindered the growth of secondary cleavages, consequently enhancing the total absorbed energy during fracture.

Ganesh et al. [30] have compared the effect of two different welding processes [multi-pass tungsten inert gas (MPTIG) and an activated tungsten inert gas (ATIG)] on thermo-mechanical behaviour of 316LN stainless steel-welded joints. Authors reported ATIG

joints possessed higher toughness and elongation as compared to MPTIG and attributed such behaviours to controlled heat input and lesser δ-ferrite contents.

Nishimoto and Mori [31] while investigating hot cracking tendencies in laser beam welding of high nitrogen stainless steels, correlated cracking susceptibility to nitrogen content and solidification rates. With the increase in solidification rates, primary austenite was found to be a dominant solidification mode which resultantly exacerbated hot cracking. Similarly, Jie Ning et al. [32] drew a comparison of Laser-MIG hybrid and M.I.G. welded High nitrogen austenitic stainless steel. Hybrid configuration of Laser-MIG showed better tensile properties and more retained impact absorption energy in comparison to M.I.G. welded joints. Authors attributed this behaviour to more retained solid solution strengthening effect resulted by comparatively high nitrogen content in Laser-MIG hybrid joint.

The motivation for this work stems from the limitations of traditional welding methods such as T.I.G., ATIG, M.I.G., and laser welding, which are commonly used for various types of stainless steels. These methods often lead to challenges such as high heat input, distortion, and undesirable microstructural changes, particularly in nitrogen-strengthened austenitic stainless steels (LNiASS). Electron Beam Welding (EBW) offers a promising alternative due to its high energy density, vacuum environment, and minimal distortion. Despite its potential, E.B.W. remains underexplored for LNiASS. This study aims to fill this gap by analyzing the Microstructure, mechanical properties, and residual stresses in EBW-welded LNiASS joints. By demonstrating the advantages of E.B.W. in preserving mechanical properties, minimizing distortion, and reducing the risk of sensitization, this research seeks to provide valuable insights into the effectiveness of E.B.W. for nitrogen-strengthened stainless steel, thereby advancing the field of welding technology. The present work investigates the microstructural evolution, phases formation in the FZ, mechanical properties relationship based on Microstructure, and residual stresses of electron beam welded nitrogen-strengthened austenitic stainless steels (LNiASS).

2. Materials and methods

2.1. Material

The alloy under consideration is a nitrogen-strengthened low nickel austenitic stainless steel with measured composition by energy dispersive spectroscopy (EDS) as given in Table 1. Similar composition is reported in the literature.

Electron beam welding was performed in one-pass autogenous mode. Before welding, preliminary experimental runs were carried out in bead-on-plate configurations. Absolute penetrations were achieved for a minimum beam current value of 16 mA for a 1 mm thick sheet. Later, weld formation and the weld integrity were explored with welding parameters in Table 2.

'Modified Suutala's and 'Extended WRC-1992 (Kotecki and Siewert)' constitutive diagrams constitutive diagrams were employed to accurately map solidification products and better predict the ferrite content and solidification modes.

2.2. Microstructural characterization

To observe the microstructure evolution within the weldment, samples were sectioned transversely to the weld travel direction using wire EDM, including the weld bead. The samples were cold-mounted using epoxy for metallographic examination and subsequently ground using SiC papers ranging in 240–4000 grit size. They were then polished using 0.05 μm alumina particle paste on a ferrous velvet cloth. Samples were electrolytically polished for 30 s at 5 V and etched for 20 s at 10 V using an electrolyte solution of 40 g Oxalic acid in 100 ml distilled water to reveal the optimal macrostructure and grain growth direction. Similarly, using a NaOH solution as the electrolyte (15 g NaOH in 100 ml distilled water), samples were polished at 3 V for 15 s and etched at 10 V for 15 s to obtain binary field images containing ferrite and austenite. The etched samples were observed under a polarized light microscope (Olympus BH2-UMA). The joint's microstructures, chemical composition, and fractography were examined and analyzed using a scanning electron microscope (Mira-3 Tescan PC controlled FE-SEM) under a vacuum chamber pressure of 10^6 Pa.

2.3. Mechanical testing

The specimens for tensile testing were extracted in a transverse direction from a welded sheet using a wire-EDM following ASTM standard E8/E8M-13a [34] and is shown in Fig. 1(a). Tensile tests of 03 specimenss were conducted at room temperature using a 30 kN electro-mechanical controlled Instron 5567 machine with a 1.5 mm/min crosshead speed.

A Micro Vickers Hardness test was performed in accordance with standard ASTM-E384-22 [35], using a microhardness tester, TUKON Model TU 300. A pyramidal diamond indenter with a face angle of 136° was used to apply a load (P) of 1.961 N (200 gf) with a dwell time of 15 s at room temperature. The hardness was measured along the weld bead, including the base metal (BM), HAZs, and FZ.

Impact testing was performed at room temperature to evaluate the toughness of the weldment and BM with 3 specimens each in the V-Notch Charpy configuration using a BROOKS Pendulum Impact Testing machine. The specimen dimensions were ensured to be in

Table 1
Composition of Alloy (Alloying elements in wt.%) [33].

C	Cr	Mn	Ni	Cu	Si	P	S	N	Fe
0.07–0.075	16	9.5	1.1	1.6–1.7	0.4	0.05	0.005	0.28	Bal.

Table 2
Electron beam welding parameters.

	Accelerating Voltage (kV	Focusing Current (A)	Beam Current (mA)	Welding Speed (mm/min)	η EBW	Weld Power (J/sec)	Heat Input (J/mm)<
Tack pass	50	91	6	1000	–	–	–
Weld Pass	50	91	16	1000	0.95	760	45.5

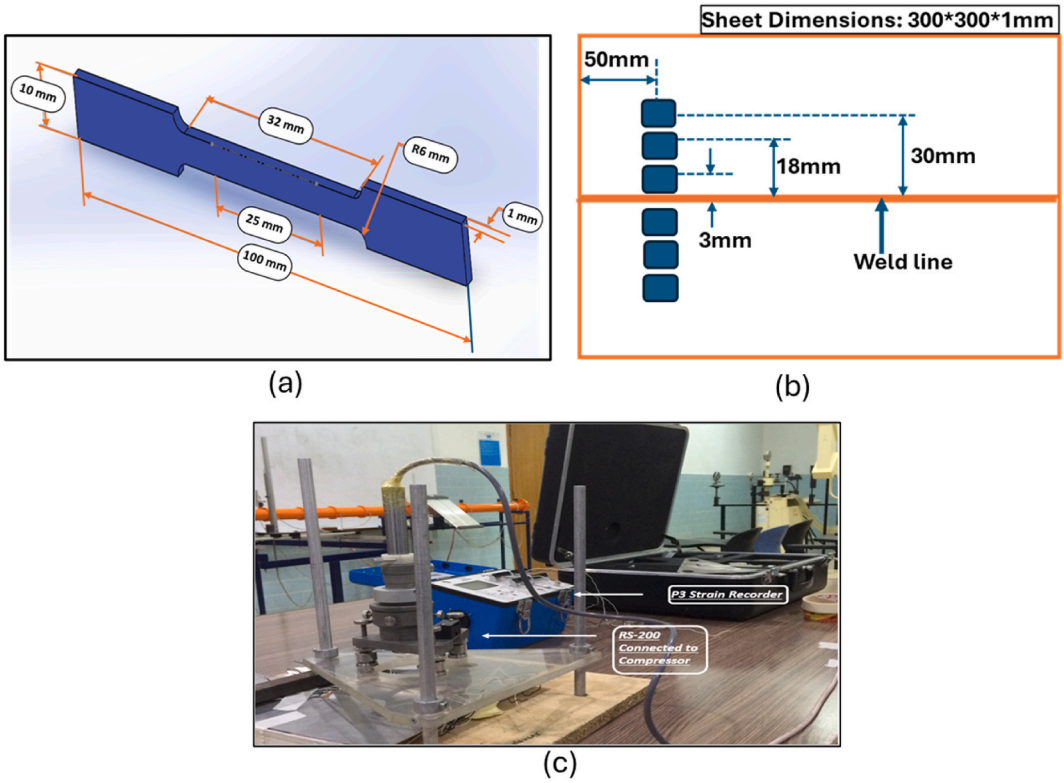

Fig. 1. (a) Dimensions of tensile test specimen obtained from the weldment. (b) Locations of residual stress measurements for the welded plate. (c) Experimental Setup for Residual Stress Measurements.

accordance with the standard ASTM E23-18 [36].

2.4. Residual stress evaluation

The Hole Drill Strain Measurement (HDSM) method i.e. ASTM E−837-20 [37] was utilized to measure the residual stress distribution in the weldments. A three-element strain gauge rosette (B 062UM-120 Ω) was positioned and cemented over each point of concern on the weld-stressed plate, as shown below in Fig. 1(b).

A 1.6 mm diameter hole was drilled at the center of each rosette using a high-speed pneumatic drill (model RS-200 by Vishay Measurement Group, Raleigh, NC, U.S.A.). Depth increments were achieved with a feed rate following standard procedures to minimize friction-induced thermal effects. The drilling operation was performed intermittently, with the drill being continuously touched and removed.

In order to comply with ASTM E837-20 [37] standard stipulation, instrumentation selected for recording of strains had a strain measurement resolution of ±1 μm/m or 1 micro strain as shown in Fig. 1(c). For this purpose, 'Micromeasurements V·P.G.' strain recorder 'P3' was employed. In-built quarter-bridge was configured to each individual rosette to complete a fully balanced Wheatstone bridge circuit. Aim to adopt such configuration during experimentation is to ensure sensitiveness while recording strain values.

The locked-in stresses were determined from the relieved strains ε1, ε2 and ε3. Relieved strain values were read by the strain gauge rosettes. Commercially available H-Drill® software was employed to find the calibration constants from provided geometry and hole depth.

3. Results and discussions

3.1. Weld bead profile analysis

The micrograph presented in Fig. 2 illustrates the cross-sectional view of a crack-free welded joint produced through an autogenous Electron Beam Welding (EBW) process. The fusion zone appears uniform and symmetrical, devoid of discernible mismatch at the abutting ends. Macroscopically, the weld exhibits a broad upper region and a narrower root region, indicating a weld free from significant defects. The observed pooling of molten metal toward the upper portion of the weld can be attributed to the configuration of the electron beam operating in keyhole mode during welding [38,39]. Moreover, the weld's pronounced toe profile is attributed to the optimal beam current (I) settings and adequate sidewall fusion across the weld bead configuration experiments, resulting in consistent full-penetration welds [40].

The welded joint consists of a microstructure that includes the FZ, the HAZ, and the BM, as shown in Fig. 2. The width of the fusion zone tapers from 1.45 mm at the top of the plate to approximately 0.9 mm at the bottom. The width of the HAZ extends about 0.4 mm–0.6 mm beyond the fusion boundary on both sides.

3.2. Ferrite content and solidification analysis

Solidification analysis and cracking susceptibility analysis were conducted, considering the composition and the effects of rapid solidification. Employing feasible constitutive diagrams, including one proposed as 'Modified Suutala's' and 'WRC-1992(Kotecki and Siewert)' [41] serve well for this purpose. Moreover, Cr_{eq} and Ni_{eq} as per formulated in WRC-1992, are calculated using the Eq [1] and Eq [2]:

$$Creq = \%Cr + \%Mo + 0.7(\%Nb) \quad \text{Eq[1]}$$

$$Nieq = \%Ni + 35(\%C) + 20(\%N) + 0.25(\%Cu) \quad \text{Eq[2]}$$

According to WRC-1992, the Ni equivalent (Nieq) does not account for the effect of manganese content on stabilizing the austenite structure against ferrite. These boundaries limit the possibility of martensite formation since manganese, as an alloying element, is more effective at inhibiting martensite formation rather than stabilizing austenite against ferrite. The solidification mode and ferrite contents are presented in Table 3.

A similar approach towards solidification mapping while taking solidification rates and equivalency ratio into account has been adopted by Hochanadel et al. [42]. The solidification path and corresponding Microstructure of F.A., as a result of reaction during solidification, is shown as;

$$L \rightarrow L + F \rightarrow L + F + (F + A) \rightarrow F + A$$

The primary solidification mode of F.A. is significant because it results in a two-phase mixture of austenite and ferrite along the solidification grain boundary (SGB), which helps prevent crack propagation. Additionally, the solidification path depends on transformation kinetics; the weldment can retain ferrite in varying amounts, from a few volume percentages to ferrite as the primary solidification product with austenite in the interdendritic regions, depending on the Creq and Nieq values. Ferrite and δ-ferrite both have a B.C.C crystal lattice, in contrast to austenite, which has an F·C·C crystal lattice. Moreover, these crystal lattice configurations differ in volume.

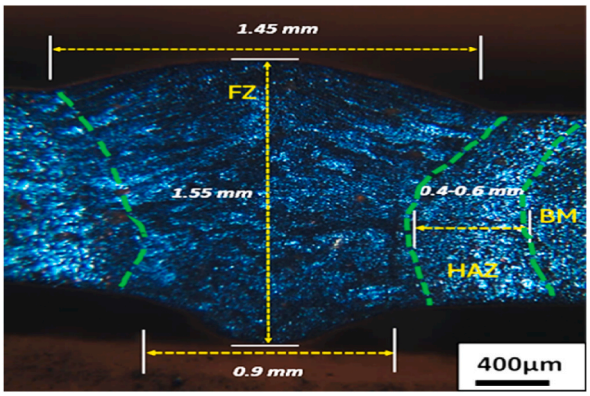

Fig. 2. Microstructure of single pass autogenous E.B. welded joint.

Table 3
Solidification products.

	Cr_{eq}	Ni_{eq}	Equivalency Ratio	Solidification Mode	Ferrite Content (%)
WRC-1992 (Kotecki and Siewert)	16	9.95	1.6	FA (Primary ferrite transformed to austenite)	2–4

3.3. Microstructural analysis

3.3.1. Microstructure

Fig. 3(a) shows the optical micrograph of the weldment, including the FZ, partially melted heat-affected zone (PMHAZ), coarse-grained heat-affected zone (CGHAZ), and BM. The grains in the PMHAZ are relatively finer than those in the CGHAZ, as shown in Fig. 3(b), which might be due to the variation in heat input during the welding process. The heat input during the E.B.W. process plays a crucial role in the microstructural evolution of the welded joint. Heat input, calculated as the product of the electron beam power and welding speed, directly influences the thermal cycles experienced by the alloy. This, in turn, affects phase transformations, grain growth, and precipitation behavior within the fusion zone and HAZ. The FZ demonstrated various solidification morphologies within the weld pool after welding. The top region is comprised of epitaxial dendritic growth, as shown in Fig. 3(c), which extends between the weld center and fusion boundary due to the heat flow or heat extraction direction and thermal gradients at the solid-liquid front during solidification [9,43]. Dendritic growth seems to commence at this parting line approach fusion boundaries on both sides. The prominent columnar grains near the top of the weld bead could be due to the extended thermal cycle, which provides ample span for grains to grow and coarsen.

Moreover, lateral heat flow and associated dendrite growth occurred in a direction perpendicular to the fusion boundary. The region below the mid-thickness proximity exhibited equiaxed morphology during the solidification cycle, as highlighted in Fig. 3(.) and magnified image in Fig. 3(d). This can be attributed to the relatively confined volume and higher cooling rates compared to the dendritic growth regions.

As depicted in Fig. 4(a, b, and c), the microstructural analysis of the FZ, at higher magnifications reveals a complex dendritic structure characterized by distinct morphologies of δ-ferrite within an austenite matrix. The primary morphologies identified include skeletal δ-ferrite, vermicular δ-ferrite, and lathy δ-ferrite. These morphologies are significant as they influence the welded joint's

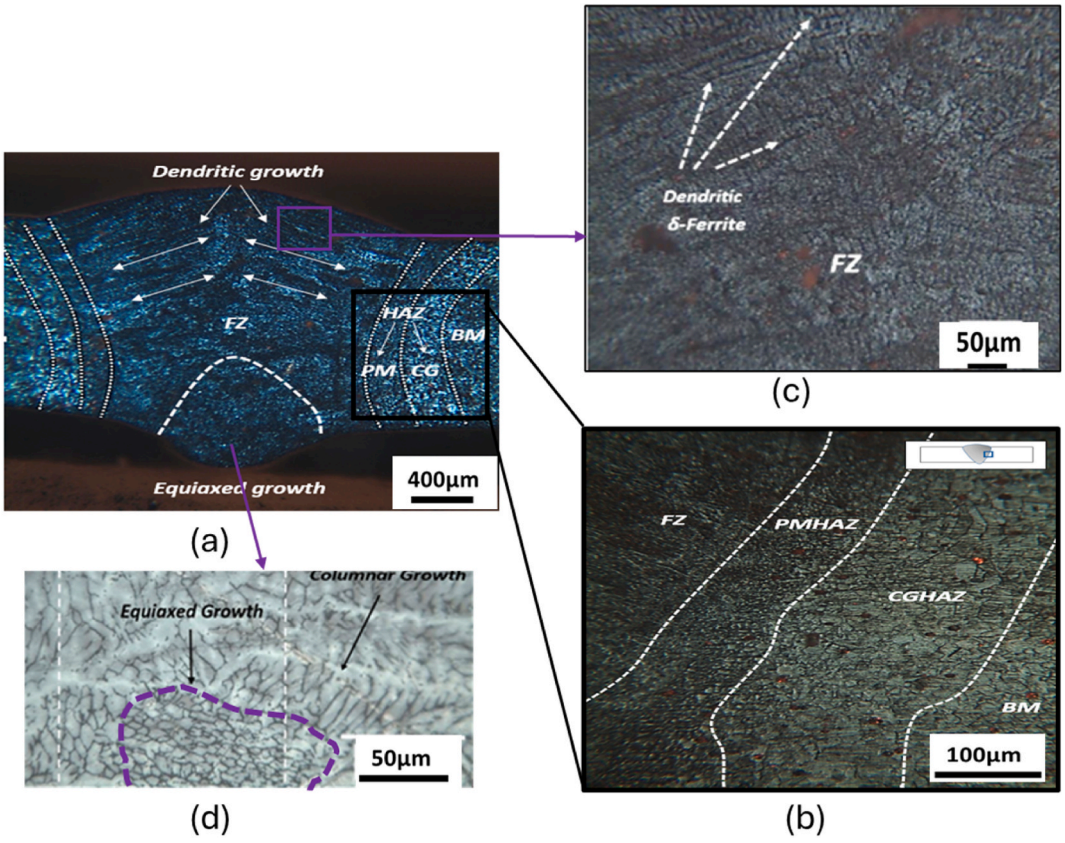

Fig. 3. (a) Optical micrograph of weldment (b) FZ with Partially melted HAZ and coarse grain HAZ. (c) FZ. with Equiaxed and columnar grains (d) FZ with dendritic morphology.

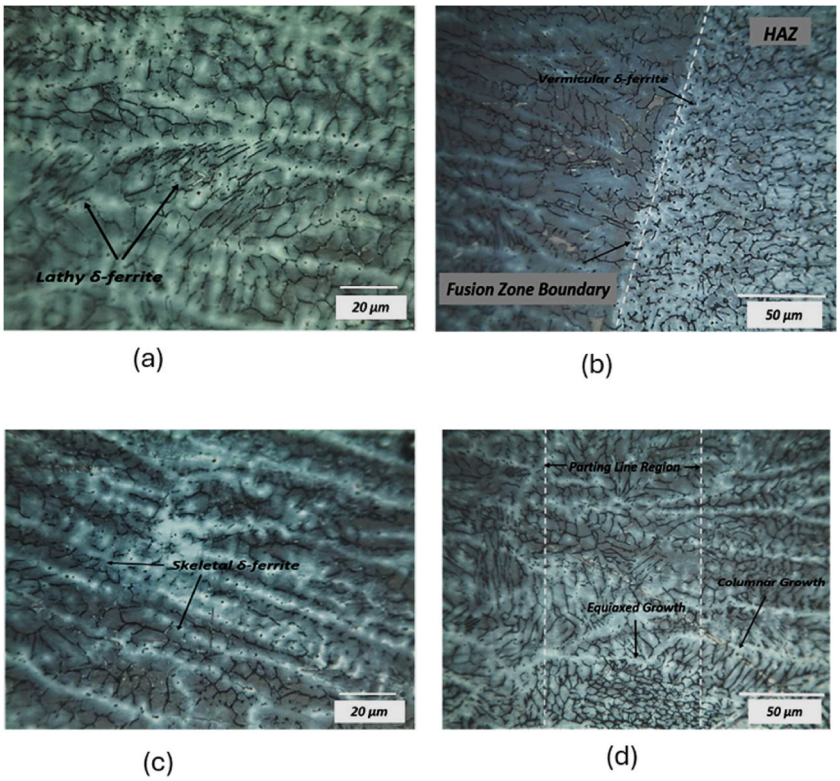

Fig. 4. Optical micrograph Images showing (a) Presence of Lathy δ-ferrite (b) Vermicular δ-ferrite on transition boundary (c) Skeletal δ-ferrite morphology (d)Parting region suspended in mid of fusion zone.

mechanical properties and overall stability. Lathy δ-Ferrite, as shown in Fig. 4(a), lathy δ-ferrite consisted of thin, plate-like structures dispersed within the austenite matrix. This morphology is prevalent in the solidified weld region, indicating moderate cooling rates where δ-ferrite forms as a primary phase before transforming into the austenitic structure. Fig. 4(b) illustrates the vermicular δ-ferrite, which appears as worm-like structures confined primarily to the boundary regions between the HAZ and the FZ. The vermicular δ-ferrite is suspended towards either side of the boundary, suggesting a transitional phase that forms under specific thermal gradients and cooling rates experienced during the welding process. Skeletal δ-Ferrite morphology, evident in Fig. 4(c), consists of irregular, branched structures that resemble a skeletal framework. Skeletal δ-ferrite is typically observed in the solidified weld region. Its presence indicates rapid solidification conditions, where the δ-ferrite forms as a primary phase and is subsequently encased by the austenite matrix. Similar Microstructure has been reported by the various authors [44,45].

The ferrite phase can also be seen in the HAZ (Fig. 4(b)), which could have resulted from the dissolution of Nitrogen from the HAZ into the fusion zone, leaving behind nitrogen-deprived regions in the HAZ (Nitrogen being an austenite stabilizing element). The dissolution process of Nitrogen from the HAZ to the FZ is well illustrated by Liu et al.l [46]. In addition, cellular austenite in the fusion zone can be witnessed commencing at the bottom and depth-wise mid of the fusion zone. At the same time, columnar dendrites can be well seen spreading next to it and across the horizon of weld, as shown in Fig. 4(d).

Fig. 5(a) in the fusion zone reveals primary dendrites, which appear to be relatively widely spaced towards the top of the weld. On

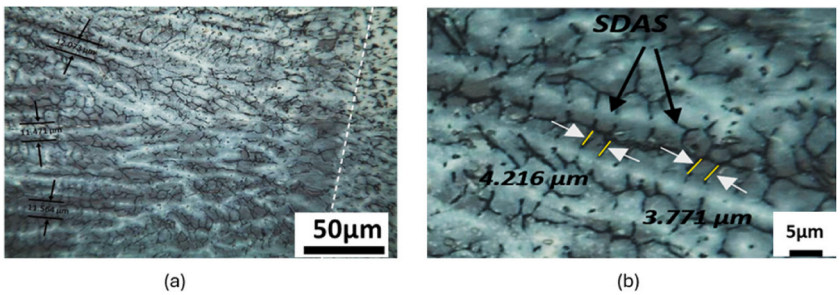

Fig. 5. (a) Primary dendrite arm spacing (λ1). (b) Secondary dendrite arm spacing (λ2).

average, the spacing between these primary dendrites was 11.774 μm. The spacing of primary dendrites, known as primary dendrite arm spacing (PDAS), is primarily influenced by the heat input and cooling rate. Typically, a higher cooling rate and lower heat input lead to a refinement of PDAS [47]. Moreover, the average spacing between secondary dendrite arms was 4.077 μm, as shown in Fig. 5 (b). The difference in dendrite arm spacing for both primary (λ_1) and secondary (λ_2) branches indicated variations in solidification time. This variability in dendrite coarsening and its sensitivity to changes are influenced by the local solidification time, as noted by Donadoni et al. [48].

3.4. Variation in composition and pore formation

S.E.M. micrographs displayed in Fig. 6 (a and c) illustrate the HAZ and FZ of the weldment. Notably, multiple micro-pores are evident in the HAZ, as depicted in.

Fig. 6(b) and (d). These micro-pores are attributed to the rapid solidification behavior of high-energy-density welding processes, which tend to oversaturate the nitrogen content in the weld pool. Consequently, nitrogen pore nucleation occurs upon solidification [46,49].

In addition, the majority of the pores ~1 μm in size were present at the grain boundaries, with some pores < ~1 μm within the grains, which can be attributed to any trapped gases, such as Nitrogen, which may form micropores due to the inability to escape the solidifying metal matrix [50].

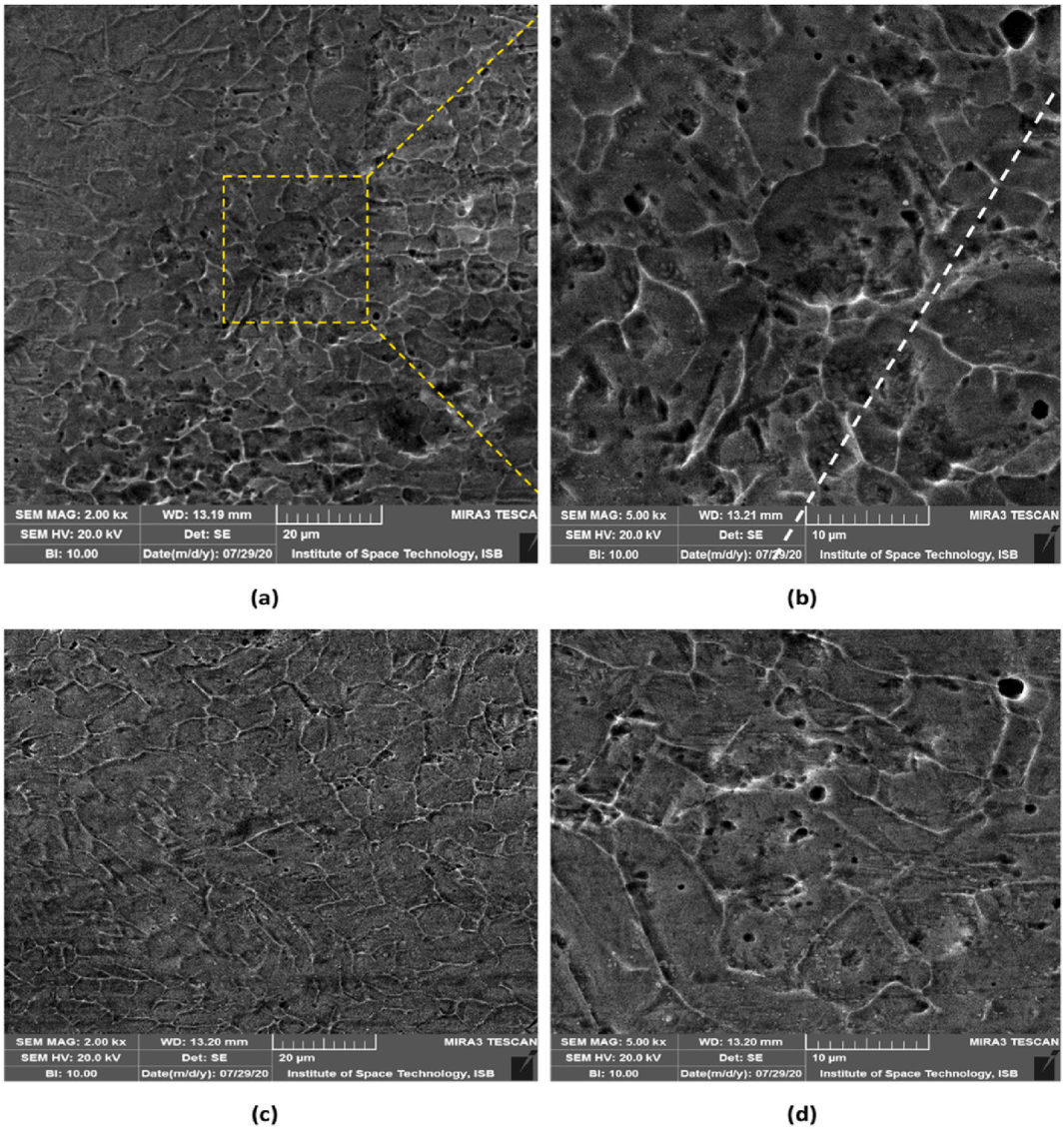

Fig. 6. (a) & (b) SEM images showing nitrogen Pore nucleation at HAZ; (c) & (d) Fusion zone of the weldment.

The E.D.S. analysis presented in Fig. 7(a, b, c) provides crucial insights into the elemental distribution and compositional changes across different regions of the weldment. Specifically, the analysis revealed a notable decrease in manganese (Mn) content from the BM through the HAZ and into the FZ. The Mn content dropped from 9.93 % in the BM. to 9.55 % in the HAZ and further decreased to 6.55 % in the FZ. This gradation in Mn concentration indicates significant compositional changes induced by the welding process.

The reduction in Mn content within the FZ can be attributed to several metallurgical phenomena. Firstly, Mn has a high affinity for Nitrogen, leading to the preferential formation of nitrides. During welding, the intense heat input causes Nitrogen to migrate from the high-temperature fusion zone to regions with a higher concentration of nitride-forming elements, such as Mn. This migration results in localized depletion of Mn in the FZ, as it is consumed in the formation of nitrides. Moreover, as an interstitial element, Nitrogen diffuses readily under the thermal gradients established during welding. The higher affinity of Mn for Nitrogen facilitates the formation of stable nitrides in regions where Mn concentration is relatively higher. This results in the reduction of free nitrogen content in the FZ, where Mn has been depleted, consequently affecting the mechanical properties of the welded joint.

The EDS analysis, presented in Fig. 7(a, b, c), provides crucial insights into the elemental distribution and compositional changes across different regions of the weldment. Specifically, the analysis revealed a notable decrease in manganese (Mn) content from the BM through the HAZ and into the FZ. The Mn content dropped from 9.93 % in the BM to 9.55 % in the HAZ and further decreased to 6.55 % in the FZ. This gradation in Mn concentration is indicative of significant compositional changes induced by the welding process.

The reduction in Mn content within the FZ can be attributed to several metallurgical phenomena. Firstly, Mn has a high affinity for Nitrogen, leading to the preferential formation of nitrides. During the welding process, the intense heat input causes Nitrogen to migrate from the high-temperature fusion zone to regions with a higher concentration of nitride-forming elements, such as Mn. This migration results in localized depletion of Mn in the FZ, as it is consumed in the formation of nitrides [51]. Moreover, Nitrogen, being an interstitial element, diffuses readily under the thermal gradients established during welding. The higher affinity of Mn for Nitrogen facilitates the formation of stable nitrides in regions where Mn concentration is relatively higher. This results in the reduction of free nitrogen content in the FZ, where Mn has been depleted, consequently affecting the mechanical properties of the welded joint.

3.5. Mechanical evaluation

3.5.1. Microhardness results

Fig. 8 presents the microhardness profile across the weldment, including the HAZ and FZ, at three locations: 0.2 mm, 0.5 mm, and 0.8 mm from the top surface of the specimen, as shown in the inset of Fig. 8. The hardness values follow a decreasing trend from the middle of the fusion zone toward the fusion boundary, HAZ, and finally the BM. The hardness values for the BM range from 207 HV0.2 to 211 HV0.2 across all three depths. The hardness values recorded for the HAZ regions were approximately 5.26 % higher than those of the BM but about 7.27 % lower compared to the hardness in the fusion zone.

Similarly, for the FZ, values vary between 235 HV0.2 to 237 HV0.2 for the top location at 0.2 mm from the top surface, which is 12.92 % higher than the BM For the location at 0.5 mm and at 0.8 mm depth, the values seem to vary between 240 HV0.2 to 242 HV0.2 and 239 HV0.2 to 241 HV0.2, respectively. The increase in hardness can be associated with the rapid solidification of the molten weld pool, resulting in finer grains that yield enhanced hardness values. Moreover, the fast cooling rate provides insufficient time for the

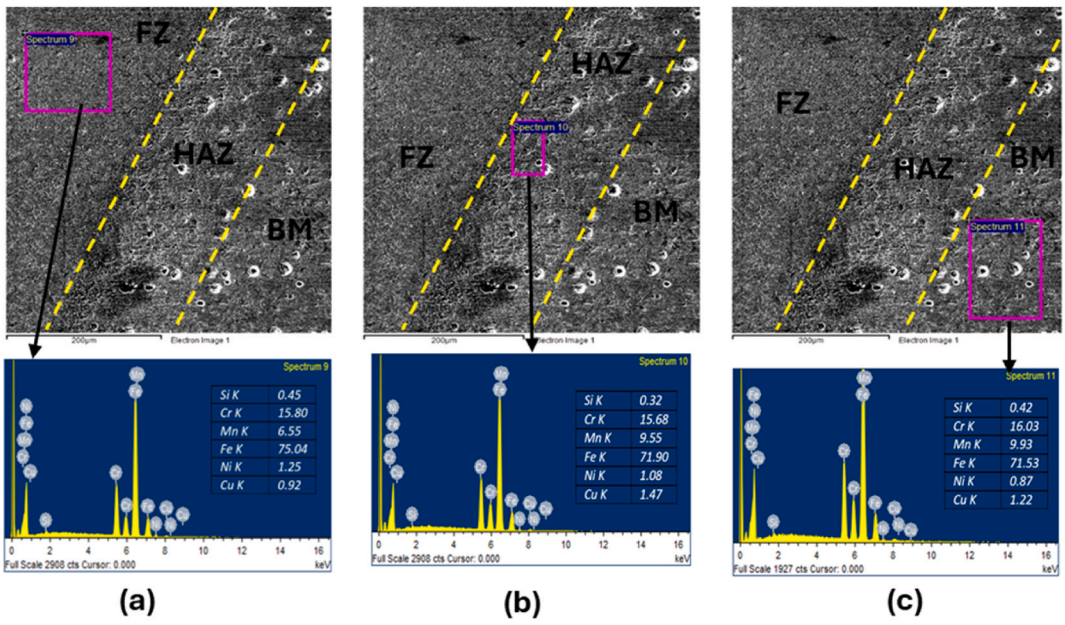

Fig. 7. E.D.S. analysis of (a) FZ (b) HAZ and (c) BM.

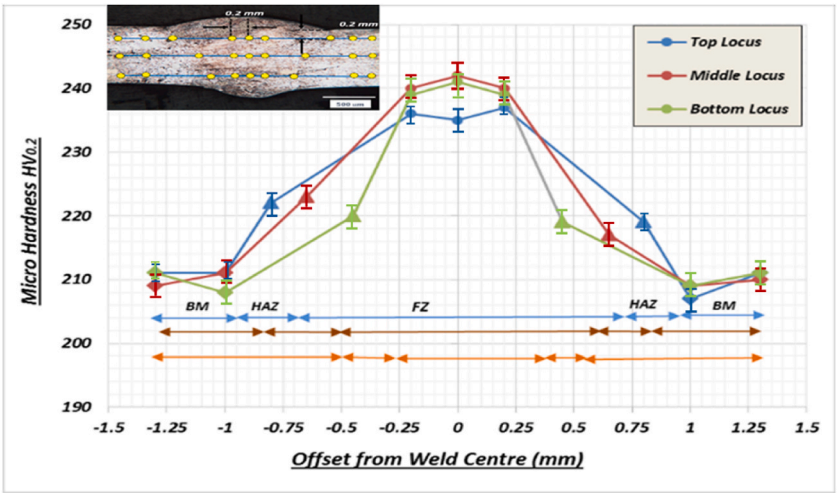

Fig. 8. Microhardness profiles across the transverse section of the weldment.

existing high-temperature phases to transform back to austenite. A similar trend was observed in previous studies [52,53]. Further, the dendritic structure can be characterized as fine equiaxed dendrites or fine columnar dendrites, both of which improve hardness owing to their finer grain structure.

3.5.2. Tensile testing results

Uniaxial tensile tests were performed on BM specimens and three electron beam welded specimens, with results presented in Table 4. The tensile strength of the BM was recorded at 918.5 MPa, while the weldments ranged from 712 MPa to 807 MPa. A similar descending trend was observed for yield strength, where the weld metal yield strength was approximately 9 % lower than the base alloy. The decrease in strength can be attributed to several factors, including the vaporization of alloying elements such as manganese and Nitrogen and microstructural changes in the welded regions. During welding, alloying elements vaporize based on their vapor pressure, with Nitrogen, being a lighter element with very high vapor pressure, escaping from the weld well before solidification. Such losses can be significant, reaching as high as 30 % during arc welding [54]. Thereby, the extent of concentration loss shall have a detrimental effect on strength as well as the solidification structure of the weld material [55]. In addition, welded specimens had shown ~50 % decrease in elongation, owing to the grain growth and formation of δ-ferrite as a secondary phase within HAZ, led to the early initiation of crack under loading [56]. Moreover, coarse grains provide an easy passage for voids to nucleate and subsequently fracture to occur soon.

Tensile fractured specimens are shown as insets in Fig. 9. The BM specimen's fracture occurred at a minor offset from the middle of the gauge length, while welded specimens were fractured from HAZ immediately next to the weld joint.

3.5.3. Impact testing results

Single-notch specimens of all the BM and welded specimens were prepared for the impact testing and the results are presented in Fig. 10. It is evident from table that the welded specimens had 50 % higher notch toughness and resistance to crack propagation than BM, owing to the plasticity.

Induced by the formation of a higher proportion of austenitic and (2–4%) of δ-ferrite during the cooling cycle of the welding process. Moreover, the BM specimen offered significantly lower resistance towards crack propagation than resistance offered by the weld metal specimen since the introduced notch lies in the absolute middle of the specimen and is in-line with the weld cord.

3.6. Residual stress results

Welding-induced residual stresses near the weld seam significantly influence brittle fracture, fatigue crack propagation, and resistance to structural instability. Generally, a very narrow zone under the electron beam is abruptly heated compared to its surroundings, leading to localized fusion and vaporization during beam penetration. Elevated temperature gradients during and after the

Table 4
Comparison between BM and welded joint.

	Yield Strength (MPa)	Tensile Strength (MPa)
Base Metal	406 ± 8	918.5 ± 12
Weld joint	368 ± 8	770 ± 9
% reduction	9.36	16.17

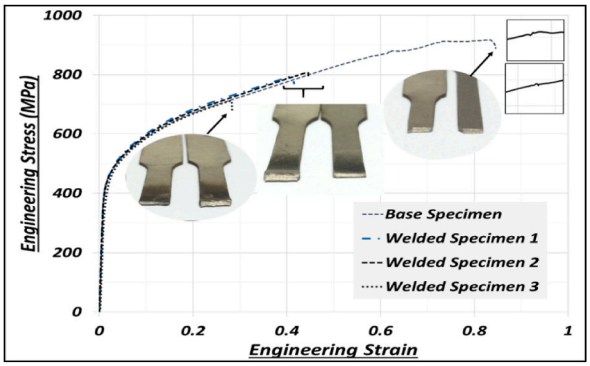

Fig. 9. Stress-strain curves of BM and welded joint Specimens (standard deviation: ± 2 MPa).

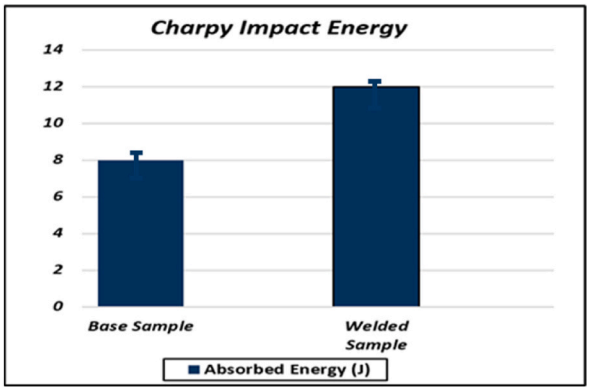

Fig. 10. Absorbed impact energy of the welded joint and BM sample.

weld-thermal cycle cause non-uniform thermal strains and volumetric changes due to secondary phase formation. This phenomenon ultimately results in cumulative residual stress profiles in the weldment and associated regions [57,58].

Generally, during welding of austenitic stainless steels δ-ferrite, being the high-temperature phase and existing at elevated temperatures, is not allowed to transform back to parent austenite while rapid cooling completely. Therefore, it tends to stay in the weld pool afterward. This addition to existing and uniformly distributed F·C.C. austenite shows a tendency towards volumetric change, eventually causing induced stress. Moreover, the difference in the coefficient of thermal expansion of austenite and ferrite [59] further complicates the comprehension of residual stress profiles in a pool of binary phases and, hence, regions associated with the weld. Eventually, these microstructural changes, along with thermal cycle induced strains, contributed to the overall stress state of weldment and its vicinity in a rather complex way.

Figs. 11 and 12 depicts the distribution profile of transverse and longitudinal residual stresses (R.S.T. and R.S.L.) for the weldments

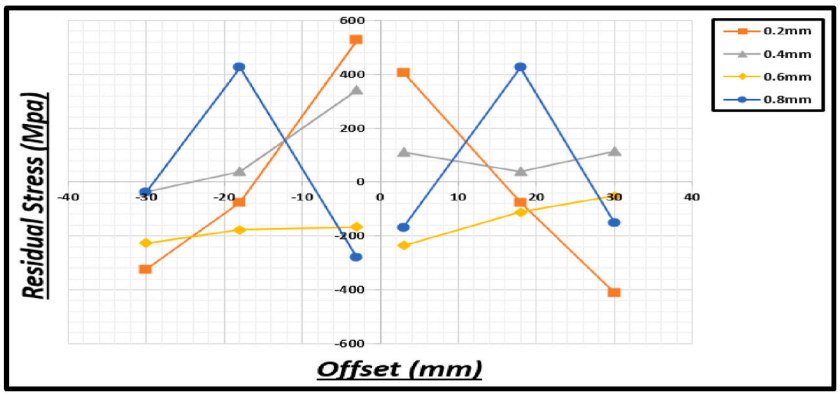

Fig. 11. Distribution profile for longitudinal component of residual stresses (standard deviation: ±1.5 MPa).

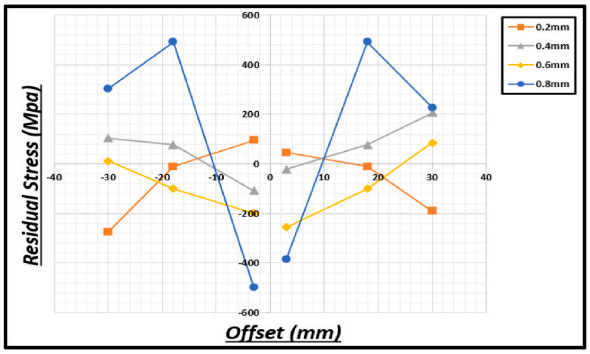

Fig. 12. Distribution profile for transverse component of residual stresses (standard deviation: ±2 MPa).

obtained through integral method proposed by Grant et al. [60] at varying depths.

For 50 mm locus and 0.3 mm offset, the ~400 MPa tensile (R.S.L.) were seen closest to the weld cord at near top surface region i. e 0.2 mm depth. On the other hand, for the same measurement point positioned at 3 mm offset, the magnitude of longitudinal stress keeps on decreasing down the depth and attains compressive nature below the mid thickness. The highest magnitude of compressive residual stress was at the farthest measurement from weld bead and taken at 0.2 mm from the top surface.

Although the stresses near the top surface at 0.2 mm depth were highly tensile, they reduced drastically as the measurement point moved away from the weld bead. This abrupt descending trend near the weld bead, i.e., the HAZ, is linked to the mismatch between the yield strengths of both the FZ and the HAZ. This observation aligns with the distribution of residual weld stresses in the weldment, where these stresses are predominantly tensile near the weld bead and compressive in regions farther away, thereby balancing the opposing tensile stresses.

3.7. Fractography

For the tensile failure occurring in the HAZ, the fracture surface demonstrates the transition between two major fracture topographies as shown as insets in Fig. 13(a). The fracture from the HAZ can be associated with coarse grain morphology produced during the welding process and the stress with respective strains to nucleate microvoids decreases with increasing grain size [61]. The weld pool width at weld top is greater than width at weld bottom therefore the sectioned view i.e. fracture surface, contains the chunk of both mixed fracture and pure ductile fractured region.

The SEM images focused on ductile failure zones revealed a network of cup-and-cone patterned ridges and dips, characteristic of ductile failure through microvoid coalescence. Microvoids generally form around existing or suspended tiny inclusions or gas pores under stress, causing them to stretch and open. These microvoids eventually merge to create larger voids, which ultimately lead to cracks significant enough to cause fracture. The ridges and dimples between the voids, as shown in Fig. 13(c) and (d), are the last locations to deform. Under stable ductile tearing, a crack in a ductile material often propagates for a few millimeters or even microns before final rupture or a brittle fracture. When examined at higher magnification, microvoid coalescence is identified as the primary failure mechanism. Brittle fracture sites, appearing as faceted areas within the fracture horizon and in Fig. 13(b), can be observed cutting through the grains in a transgranular manner. Moreover, mixed fracture results have been reported for hybridized welding approaches undertaken for high nitrogen austenitic stainless steel [32], and finite element-powered approaches have endorsed this phenomenon [62].

4. Conclusions

Thin plates of low-nickel nitrogen-strengthened austenitic stainless steel were joined by the electron beam welding technique and following conclusion were drawn.

1. Various ferrite morphologies were identified, such as skeletal, lathy, and vermicular structures. No significant precipitation of deleterious phases (carbides and sigma phases) was observed. The absence of cracking during solidification was associated to the ferritic solidification mode (F.A.). These findings demonstrate the stability and integrity of the weld microstructure, providing confidence in the weld's resistance to phase-induced brittleness and solidification cracking.
2. The weldment exhibited a strength approximately 90 % of that of the base alloy samples. Fractures were observed in the immediate vicinity of the weld cord, primarily due to the tangible loss of Nitrogen from the weld-associated regions and grain coarsening in the HAZ This result underscores the critical impact of nitrogen loss and grain coarsening on the mechanical properties of the welded joints, providing insights for improving weld quality.
3. The microhardness of the weldment was found to be 12.9 % higher than that of the base alloy. This increase is attributed to microstructural evolution and the presence of a fine-grained structure with an interdendritic spacing of 4.771 μm. The fine grain

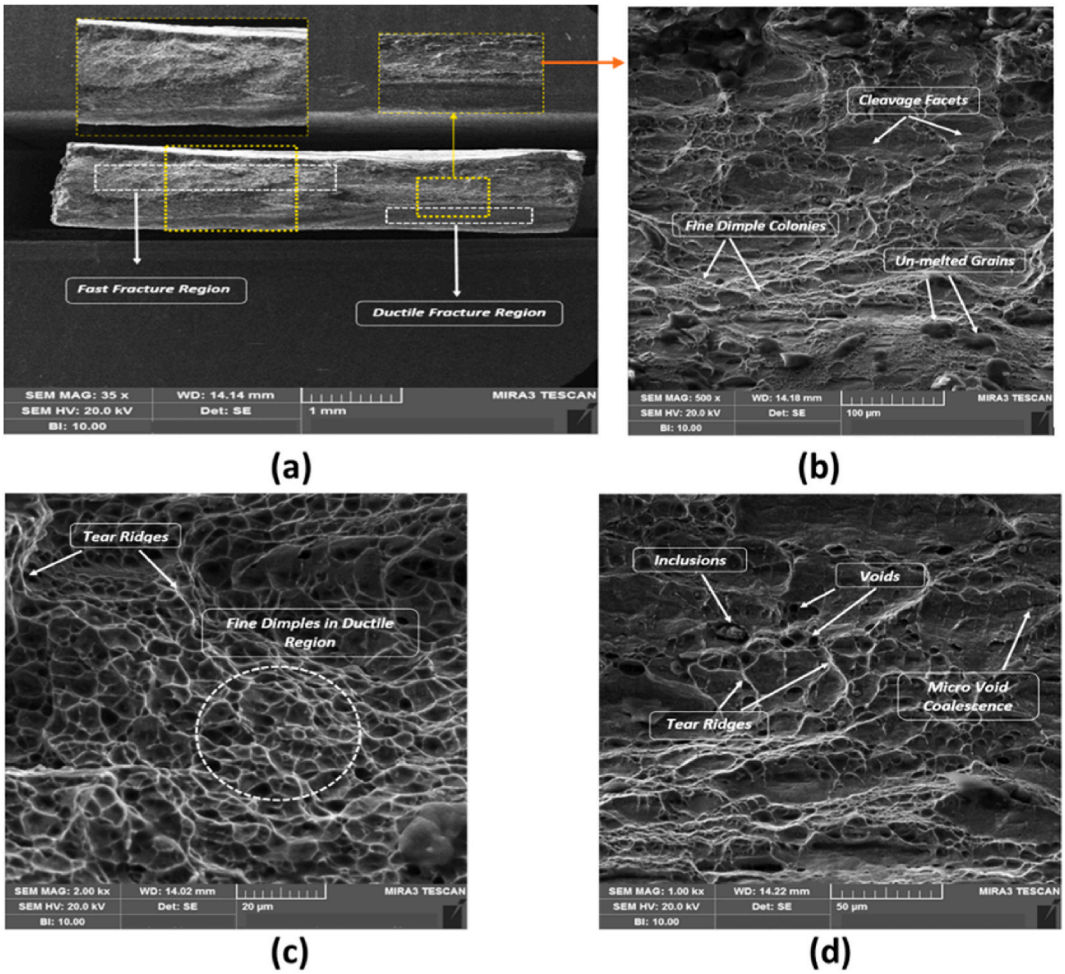

Fig. 13. Fractured surface of tensile specimen with insets showing transition between two topographies.

boundaries act as barriers to dislocation movement, enhancing the material's hardness. This finding is significant as it demonstrates the potential for achieving higher hardness through controlled microstructural refinement.

4. Impact testing using the Charpy V-Notch (CVN) configuration revealed that the weld exhibited improved crack resistance compared to the base alloy. The weldment absorbed ~50 % higher impact energy, which is attributed to its refined Microstructure and enhanced hardness within the weld cord.
5. Longitudinal residual stress was ~400 MPa, compared to the stress in the transverse direction. The longitudinal residual stress exhibited a compressive nature below mid-thickness, attributed to the heat source travel and the extent of associated thermal expansion and contraction in the longitudinal direction. Understanding the distribution and nature of residual stresses is crucial for predicting the performance and longevity of welded structures.

Funding

This work was supported by Researchers Supporting Project Number (RSP2024R274), King Saud University, Riyadh, Saudi Arabia.

CRediT authorship contribution statement

Ahmad Naseem: Writing – original draft, Methodology, Formal analysis. **Muhammad Ilyas:** Writing – review & editing, Supervision, Formal analysis, Conceptualization. **Tauheed Shehbaz:** Writing – review & editing, Visualization, Formal analysis, Data curation. **Ghulam Hussain:** Writing – review & editing, Supervision, Resources, Project administration, Data curation, Conceptualization. **Mohammed Alkahtani:** Supervision, Resources, Project administration, Funding acquisition, Formal analysis.

Declaration of competing interest

The authors declare that they have no known competing financial interests or personal relationships that could have appeared to influence the work reported in this paper.

Acknowledgments

This work was supported by Researchers Supporting Project Number (RSP2024R274), King Saud University, Riyadh, Saudi Arabia.

References

[1] M. Rezayat, M. Karamimoghadam, M. Moradi, G. Casalino, J.J. Roa Rovira, A. Mateo, Overview of surface modification strategies for improving the properties of metastable austenitic stainless steels, Metals 13 (7) (2023) 1–27, https://doi.org/10.3390/met13071268.
[2] G. Dak, C. Pandey, A critical review on dissimilar welds joint between martensitic and austenitic steel for power plant application, J. Manuf. Process. 58 (Oct. 2020) 377–406, https://doi.org/10.1016/j.jmapro.2020.08.019. Elsevier Ltd.
[3] P. Raggi, Inflammation and calcification: the chicken or the hen? Atherosclerosis 238 (2) (2015) 173–174, https://doi.org/10.1016/j.atherosclerosis.2014.10.025.
[4] Y. He, et al., Thermal performance and experimental analysis of stainless steel flat plate solar collector with full-flow channels, Heliyon 10 (7) (2024) E28255, https://doi.org/10.1016/j.heliyon.2024.e28255, 1–14.
[5] S. Ranjan Giri, B. Kumar Khamari, B. Ranjan Moharana, Joining of titanium and stainless steel by using different welding processes: a review, Mater. Today Proc. 66 (Jan. 2022) 505–508, https://doi.org/10.1016/J.MATPR.2022.05.590.
[6] A. Thakur, A. Kumar, Recent advancements in the surface treatments for enhanced biocompatibility and corrosion resistance of titanium-based biomedical implants, Appl. Chem. Eng. 7 (1) (2024), https://doi.org/10.24294/ace.v7i1.2042.
[7] H. Vashishtha, R.V. Taiwade, S. Sharma, A.P. Patil, Effect of welding processes on microstructural and mechanical properties of dissimilar weldments between conventional austenitic and high nitrogen austenitic stainless steels, J. Manuf. Process. 25 (2017) 49–59, https://doi.org/10.1016/j.jmapro.2016.10.008.
[8] A. Soleimani, M. Akbari, A. Karimipour, A.H. Meghdadi Isfahani, R. Nosouhi, Investigation the effect of dissimilar laser welding parameters on temperature field, mechanical properties and fusion zone microstructure of inconel 600 and duplex 2205 stainless steel via response surface methodology, Heliyon 10 (4) (2024) e26010, https://doi.org/10.1016/j.heliyon.2024.e26010.
[9] Welding Metallurgy and Weldability of Stainless Steels, John Wiley, Hoboken, NJ, 2005.
[10] P. Behjati, A. Kermanpur, A. Najafizadeh, Influence of nitrogen alloying on properties of Fe318Cr312Mn3XN austenitic stainless steels, Mater. Sci. Eng., A 588 (2013) 43–48, https://doi.org/10.1016/j.msea.2013.08.053.
[11] S. Hertzman, The influence of nitrogen on microstructure and properties of highly alloyed stainless steel welds, ISIJ Int. 41 (6) (2001) 580–589, https://doi.org/10.2355/isijinternational.41.580.
[12] M. Talha, C.K. Behera, O.P. Sinha, A review on nickel-free nitrogen containing austenitic stainless steels for biomedical applications, Mater. Sci. Eng. C 33 (7) (2013) 3563–3575, https://doi.org/10.1016/j.msec.2013.06.002.
[13] An investigation of the tribological behaviour of a high-nitrogen CrMn austenitic stainless steel, Wear 215 (1–2) (Mar. 1998) 83–90, https://doi.org/10.1016/S0043-1648(97)00273-1.
[14] R.H. Espy, Weldability of nitrogen-strengthened stainless steels, Weld. J. (Miami, Fla) 61 (5) (1982).
[15] Z. Liu, et al., Optimization of the microstructure and mechanical properties of the high nitrogen stainless steel weld by adding nitrides to the molten pool, J. Manuf. Process. 49 (92) (2020) 355–364, https://doi.org/10.1016/j.jmapro.2019.12.017.
[16] W. Dong, H. Kokawa, S. Tsukamoto, Y.S. Sato, Nitrogen desorption by high-nitrogen steel weld metal during CO 2 laser welding, Metall. Mater. Trans. B Process Metall. Mater. Process. Sci. 36 (5) (2005) 677–681, https://doi.org/10.1007/s11663-005-0058-4.
[17] Weld joint properties of nitrogen-alloyed austenitic stainless steel using multi-pass GMA welding, Arch. Civ. Mech. Eng. (2020) 13.
[18] M. Ghafouri, A. Ahola, J. Ahn, T. Björk, Numerical and experimental investigations on the welding residual stresses and distortions of the short fillet welds in high strength steel plates, Eng. Struct. 260 (Jun. 2022) 114269, https://doi.org/10.1016/J.ENGSTRUCT.2022.114269.
[19] S. Das Banik, S. Kumar, P.K. Singh, S. Bhattacharya, M.M. Mahapatra, Distortion and residual stresses in thick plate weld joint of austenitic stainless steel: experiments and analysis, J. Mater. Process. Technol. 289 (October) (2021) 116944, https://doi.org/10.1016/j.jmatprotec.2020.116944.
[20] M. Junaid, K. Rahman, F.N. Khan, N. Bakhsh, M.N. Baig, Comparison of microstructure, mechanical properties, and residual stresses in tungsten inert gas, laser, and electron beam welding of Ti–5Al–2.5Sn titanium alloy, Proc. Inst. Mech. Eng. Part L J. Mater. Des. Appl. 233 (7) (2019) 1336–1351, https://doi.org/10.1177/1464420717748345.
[21] M. Abbasi, B.B. Vanani, A. Tahaei, G.L. Garagnani, Influence of Ni and PWHT on microstructure evolution and mechanical properties of GTA-welded duplex stainless steel and super duplex stainless steel joints: a comparative investigation, Proc. Inst. Mech. Eng. Part L J. Mater. Des. Appl. (2024), https://doi.org/10.1177/14644207241236743.
[22] A. Tahaei, B.B. Vanani, M. Abbasi, G.L. Garagnani, A comparison of microstructure and mechanical characteristics correlation of the joint specimens for duplex stainless steel UNS S32304 and super-duplex stainless steel UNS S32750: the role of post-weld heat treatment, Proc. Inst. Mech. Eng. Part L J. Mater. Des. Appl. (2024), https://doi.org/10.1177/14644207241233150.
[23] A. Tahaei, B. Bagheri Vanani, M. Abbasi, M. Merlin, G.L. Garagnani, The relationship between austenite stabiliser element and post-weld heat treatment on the corrosion behaviour of the welded duplex stainless steel made by gas tungsten arc welding, Mater. Sci. Technol. (2024), https://doi.org/10.1177/02670836241249829.
[24] L. Zhang, et al., Residual stress, micro-hardness and tensile properties of ANSI 304 stainless steel thick sheet by fiber laser welding, Mater. Sci. Eng., A 561 (2013) 136–144, https://doi.org/10.1016/j.msea.2012.11.001.
[25] M. Alali, I. Todd, B.P. Wynne, Through-thickness microstructure and mechanical properties of electron beam welded 20 mm thick AISI 316L austenitic stainless steel, Mater. Des. 130 (January) (2017) 488–500, https://doi.org/10.1016/j.matdes.2017.05.080.
[26] Laser beam welding of 316L T-joint: microstructure, microhardness, distortion, and residual stress, Int. J. Adv. Manuf. Technol. 8 (2017).
[27] J. Yan, M. Gao, X. Zeng, Study on microstructure and mechanical properties of 304 stainless steel joints by TIG, laser and laser-TIG hybrid welding, Opt Laser. Eng. 48 (4) (2010) 512–517, https://doi.org/10.1016/j.optlaseng.2009.08.009.
[28] Y. Ling, J. Ni, J. Antonissen, H. Ben Hamouda, J. Vande Voorde, M. Abdel Wahab, Numerical prediction of microstructure and hardness for low carbon steel wire Arc additive manufacturing components, Simulat. Model. Pract. Theor. 122 (Jan. 2023) 102664, https://doi.org/10.1016/J.SIMPAT.2022.102664.
[29] M. Mukherjee, T.K. Pal, Evaluation of microstructural and mechanical properties of Fe-16Cr-1Ni-9Mn-0.12N austenitic stainless steel welded joints, Mater. Char. 131 (2017) 406–424, https://doi.org/10.1016/j.matchar.2017.07.028.
[30] K.C. Ganesh, K.R. Balasubramanian, M. Vasudevan, P. Vasantharaja, N. Chandrasekhar, Effect of multipass TIG and activated TIG welding process on the thermo-mechanical behavior of 316LN stainless steel weld joints, Metall. Mater. Trans. B Process Metall. Mater. Process. Sci. 47 (2) (2016) 1347–1362, https://doi.org/10.1007/s11663-016-0600-6.
[31] K. Nishimoto, H. Mori, Hot cracking susceptibility in laser weld metal of high nitrogen stainless steels, Sci. Technol. Adv. Mater. 5 (1–2) (2004) 231–240, https://doi.org/10.1016/j.stam.2003.10.006.

[32] J. Ning, S.J. Na, C. hong Wang, L.J. Zhang, A comparison of laser-metal inert gas hybrid welding and metal inert gas welding of high-nitrogen austenitic stainless steel, J. Mater. Res. Technol. 13 (2021) 1841–1854, https://doi.org/10.1016/j.jmrt.2021.05.113.
[33] M. Mililitsky, N. De Wispelaere, R. Petrov, J.E. Ramos, A. Reguly, H. Hänninen, Characterization of the mechanical properties of low-nickel austenitic stainless steels, Mater. Sci. Eng., A 498 (1–2) (2008) 289–295, https://doi.org/10.1016/j.msea.2008.08.012.
[34] Test Methods for Tension Testing of Metallic Materials".
[35] M. Hardness, iTeh Standards iTeh Standards Preview Geometry into the Surface of the Material Document, i, 2022, pp. 1–15, https://doi.org/10.1520/E0384-1710-1520/E0384-22.
[36] ASTM E 23-12c, Standard test methods for notched bar impact testing of metallic materials, Standards i (2012) 1–25, https://doi.org/10.1520/E0023-12C.2.
[37] ASTM E837-13a, Standard test method for determining residual stresses by the hole-drilling strain-gage method, Stand. Test Method E837-13a i (2013) 1–16, https://doi.org/10.1520/E0837-20.1.
[38] P.S. Ghosh, et al., Progressive developments and challenges in dissimilar laser welding of steel to various other light alloys (Al/Ti/Mg): a comprehensive review, Heliyon 8 (11) (2022) E11710, https://doi.org/10.1016/j.heliyon.2022.e11710.
[39] M. Zhang, C. Wang, Z. Hua, Y. Hu, Q. Ouyang, G. Mi, Microstructure evolution, interface and mechanical properties of SiCp/2A14 joint during laser keyhole welding, J. Mater. Res. Technol. 26 (2023) 5731–5747, https://doi.org/10.1016/j.jmrt.2023.08.240.
[40] S.P. Ambade, et al., Microstructure, mechanical properties and sensitization of ultra-low nickel Cr–Mn austenitic stainless steels, J. Mater. Res. Technol. 30 (January) (2024) 4353–4365, https://doi.org/10.1016/j.jmrt.2024.04.127.
[41] D.J. Kotecki, T.a. Siewert, WRC-1992 constitution diagram for stainless steel weld metals : a modification of the WRC-1988 diagram, AWS Annu. Meet (1992) 171–178 [Online]. Available: http://www.aws.org/wj/supplement/WJ_1992_05_s171.pdf.
[42] J.E. Hochanadel, T. Patterson, J.C. Lippold, B. Panton, M.Q. Johnson, D.C. Tung, Influence of focus and deflection when comparing electron beam welds to laser welds at varying parameters in 304 SS, Weld. World 65 (5) (2021) 1007–1014, https://doi.org/10.1007/s40194-020-01046-3.
[43] N. Sayyar, V. Hansen, W.M. Tucho, M.W. Minde, Directed laser deposition of super duplex stainless steel: microstructure, texture evolution, and mechanical properties, Heliyon 9 (4) (2023) e15144, https://doi.org/10.1016/j.heliyon.2023.e15144.
[44] M. Gouné, et al., Overview of the current issues in austenite to ferrite transformation and the role of migrating interfaces therein for low alloyed steels, Mater. Sci. Eng. R Rep. 92 (2015) 1–38, https://doi.org/10.1016/j.mser.2015.03.001.
[45] Z. Dong, Y. Li, B. Lee, A. Babkin, Y. Chang, Research status of welding technology of ferritic stainless steel, Int. J. Adv. Manuf. Technol. 118 (9–10) (2022) 2805–2831, https://doi.org/10.1007/s00170-021-08128-6.
[46] Z. Liu, et al., Gas metal arc welding of high nitrogen stainless steel with Ar–N2-O2 ternary shielding gas, Def. Technol. 17 (3) (2021) 923–931, https://doi.org/10.1016/j.dt.2020.05.021.
[47] H.T. Lee, S.L. Jeng, C.H. Yen, T.Y. Kuo, Dissimilar welding of nickel-based Alloy 690 to SUS 304L with Ti addition, J. Nucl. Mater. 335 (1) (2004) 59–69, https://doi.org/10.1016/j.jnucmat.2004.06.004.
[48] B. Donadoni, G.L. de Gouveia, A. Garcia, J.E. Spinelli, A comparison of experimental time-secondary dendritic spacing and coarsening models for Al-Si-Cu alloys, J. Manuf. Process. 54 (October 2019) (2020) 14–18, https://doi.org/10.1016/j.jmapro.2020.02.047.
[49] J. Kennedy, R. Schulte, Nitrogen analysis in an electron beam welded austenitic stainless steel, Nitronic 33, J. Mater. Sci. 15 (11) (1980) 2925–2927, https://doi.org/10.1007/BF00550564.
[50] L. Zhao, Z. Tian, Y. Peng, Porosity and nitrogen content of weld metal in laser welding of high nitrogen austenitic stainless steel, ISIJ Int. 47 (12) (2007) 1772–1775, https://doi.org/10.2355/isijinternational.47.1772.
[51] N. Suutala, Effect of manganese and nitrogen on the solidification mode in austenitic stainless steel welds, Metall. Trans. A, Phys. Metall. Mater. Sci. 13 (12) (1982) 2121–2130, https://doi.org/10.1007/BF02648382. A.
[52] Metallurgical, impact and fatigue performance of electron beam welded duplex stainless steel joints, J. Mater. Process. Technol. 272 (Oct. 2019) 137–148, https://doi.org/10.1016/j.jmatprotec.2019.05.010.
[53] R. Rajasekaran, A.K. Lakshminarayanan, M. Vasudevan, P. Vasantharaja, Role of welding processes on microstructure and mechanical properties of nuclear grade stainless steel joints, Proc. Inst. Mech. Eng. Part L J. Mater. Des. Appl. 233 (11) (2019) 2335–2351, https://doi.org/10.1177/1464420719849448.
[54] J.W. Elmer, S.M. Allen, T.W. Eagar, Microstructural development during solidification of stainless steel alloys, Metall. Trans. A 20 (10) (1989) 2117–2131, https://doi.org/10.1007/BF02650298.
[55] M. Du Toit, P.C. Pistorius, Nitrogen control during the autogenous arc welding of stainless steel, Weld. World 47 (9–10) (2003) 30–43, https://doi.org/10.1007/BF03266398.
[56] V. García-García, F. Reyes-Calderón, O.D. Frasco-García, N. Alcantar-Modragón, Mechanical behavior of austenitic stainless-steel welds with variable content of δ-ferrite in the heat-affected zone, Eng. Fail. Anal. 140 (Oct. 2022) 106618, https://doi.org/10.1016/J.ENGFAILANAL.2022.106618.
[57] E.O. Hall, The deformation and ageing of mild steel: III Discussion of results, Proc. Phys. Soc. B 64 (9) (1951) 747–753, https://doi.org/10.1088/0370-1301/64/9/303.
[58] J. Ni, X. Zhuang, M.A. Wahab, Review on the prediction of residual stress in welded steel components, Comput. Mater. Continua (CMC) 62 (2) (2020) 495–523, https://doi.org/10.32604/cmc.2020.08448.
[59] M.N. James, et al., Correlating weld process conditions, residual strain and stress, microstructure and mechanical properties for high strength steel-the role of neutron diffraction strain scanning, Mater. Sci. Eng., A 427 (1–2) (2006) 16–26, https://doi.org/10.1016/j.msea.2006.03.098.
[60] Measurement Good Practice Guide No. 53 - Issue 2," p. 70.
[61] T.L. Anderson, FRACTURE MECHANICS: Fundamentals and Applications, Third Edition, 2005, https://doi.org/10.1201/9781420058215.
[62] J. Ning, K.M. Hong, G.V. Inamke, Y.C. Shin, L.J. Zhang, Analysis of microstructure and mechanical strength of lap joints of TZM alloy welded by a fiber laser, J. Manuf. Process. 39 (February) (2019) 146–159, https://doi.org/10.1016/j.jmapro.2019.02.015.